PHYSICAL REVIEW B **85**, 235441 (2012)

Tubular image states: General formulation and properties for metallic and nonmetallic nanotubes

S. Segui,[1,2] C. Celedón López,[3,4] G. A. Bocan,[1,2] J. L. Gervasoni,[1,2,4] and N. R. Arista[1,4]
[1]*Centro Atómico Bariloche, Comisión Nacional de Energía Atómica, Av. Bustillo 9500, 8400 San Carlos de Bariloche, Argentina*
[2]*Consejo Nacional de Investigaciones Científicas y Técnicas, Argentina*
[3]*Universidad Técnica Federico Santa María, Av. España 1680, Valparaíso, Chile*
[4] *Instituto Balseiro (Universidad Nacional de Cuyo y Comisión Nacional de Energía Atómica), Av. Bustillo 9500,*
8400 San Carlos de Bariloche, Argentina
(Received 15 March 2012; published 20 June 2012)

In this work we study the existence of image potential states around nanotubes by considering the interaction between a stationary charged particle and a polarizable cylinder of infinite length. For metallic nanotubes and wires we obtain the eigenstates and eigenenergies corresponding to nonzero angular momentum states, localized at a relatively long distance from the surface of the tube. We study the scaling properties of the system in order to define general conditions for which image states can be supported. We also analyze the case of nonmetallic carbon nanotubes, for which we do not obtain bound states.

DOI: 10.1103/PhysRevB.85.235441 PACS number(s): 73.21.−b, 61.46.Fg, 73.90.+f

I. INTRODUCTION

Image potential states (IPS) are surface states that result from the competition between the long-range attractive potential induced by an external charge interacting with its image and a shorter-range repulsive surface barrier. Localized outside the surface, they form Rydberg-like series of states converging toward the vacuum level.

Due to the fundamental nature of the binding potential, IPS have been reported on a variety of systems ranging from clean metallic[1,2] and semiconductor[3,4] surfaces to more exotic settings such as metal-supported metallic nanoislands,[5] the interface between certain thick films and a metallic substrate,[6] organic films,[7,8] and different carbon structures such as nanotubes,[9] fullerenes,[10] fullerites,[11] and graphene sheets.[12] A key ingredient for the efficiency of reaction processes at surfaces, their extreme sensitivity to any changes in their environment[13–18] makes them a powerful tool for probing a variety of physical and chemical phenomena at the nanometer scale.[19–21]

Among extensive theoretical work devoted to describing the formation of IPS,[22] the article by Granger *et al.*[23] predicting the existence of tubular image potential states (TIS) around nanotubes has generated considerable interest in the scientific community, and a number of papers have been published on the subject.[9,24–28] In contrast with those occurring in planar geometry, TIS are prepared with nonzero angular momentum. The resulting centrifugal barrier prevents them from collapsing into the surface of the tube, hence increasing their lifetime. This feature, together with the fact that TIS are localized around the nanotube, may facilitate their detection.

In the present work we give a thorough description of tubular image states around metallic nanotubes and extend the study to nonmetallic carbon nanotubes using a realistic model for their response functions.

The paper is structured as follows: Sec. II is devoted to describing the image potential generated by a stationary electron in front of an infinite, perfectly conductive cylinder; in Sec. III we calculate and analyze the series of bound states for this system; in Sec. IV we study the scaling properties and conditions for the formation of image states; Sec. V is focused on carbon nanotubes, both metallic and nonmetallic; finally, we summarize our conclusions in Sec. VI.

II. IMAGE POTENTIAL IN METALLIC NANOTUBES AND WIRES

An electron with charge e[29] in the proximity of a metallic infinite cylinder of radius a polarizes its surface (see Fig. 1), inducing a scalar potential Φ_{ind} given by[30]

$$\Phi_{\text{ind}}(\rho,\varphi,z) = -\frac{2e}{\pi}\sum_{m=-\infty}^{\infty}\int_0^{\infty} dk\, \cos(kz)\exp(im\varphi) \times \frac{I_m(ka)}{K_m(ka)}\, K_m(k\rho_0)K_m(k\rho), \tag{1}$$

where (ρ,φ,z) are the usual cylindrical coordinates and $I_m(x)$ and $K_m(x)$ are the modified Bessel functions. We assume the particle to be located at $(\rho_0,0,0)$, with $\rho_0 > a$. The perfectly conducting condition has been included by taking the dielectric function $\varepsilon(\omega) \to \infty$ in the general Eq. (14) of Ref. 30. In this limit, and as long as we remain outside the cylindrical surface, we can treat hollow tubes as if they were solid wires. Furthermore, this should be valid for single-walled as well as multiwalled carbon nanotubes, provided that they are metallic.

The polarized surface acts back on the external charged particle, which becomes attracted to its image charge distribution residing on the metallic surface. The "image potential" V_{im} seen by the external particle is given in terms of the induced potential as

$$\begin{aligned} V_{\text{im}}(\rho_0) &= \frac{e}{2}\Phi_{\text{ind}}(\rho_0,0,0) \\ &= -\frac{e^2}{\pi}\sum_{m=-\infty}^{\infty}\int_0^{\infty}\frac{I_m(ka)}{K_m(ka)}\,K_m^2(k\rho_0)\,dk. \end{aligned} \tag{2}$$

Figure 2 shows V_{im} as a function of the radial distance ρ_0 for a metallic, infinite cylinder of radius $a = 0.68$ nm, which corresponds to a typical single-walled carbon nanotube (SWCNT) with chiral vector (10,10). In this graph the potential (continuous line) has been calculated by adding m terms up to 10, ensuring a well-converged sum for a wide range of ρ_0.

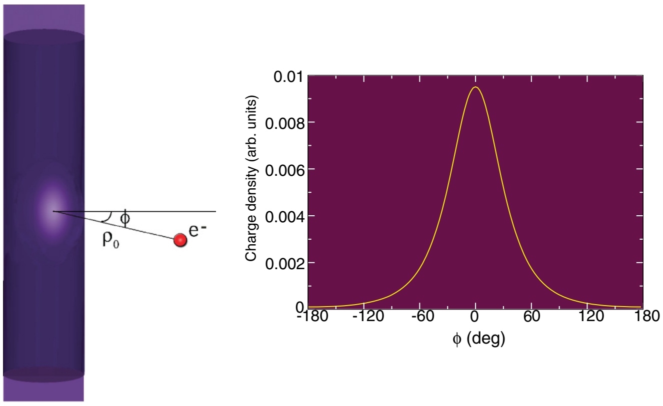

FIG. 1. (Color online) Polarization of a cylindrical metallic surface by an electron e placed at a position (ρ_0,0,0). The shadowed surface shows the charge distribution derived from Eq. (1) for the induced potential. The right panel shows the angular surface charge-density distribution at $z = 0$.

Very close to the surface an increasing number of terms were necessary in order to obtain the correct trend ($V_{\mathrm{im}} \to -\infty$ for $\rho \to a^+$). Also included in the figure is the approximation used by Granger *et al.*[23] (dashed line), given by

$$V_{\mathrm{im}}(\rho_0) \approx \frac{2}{\pi}\frac{e^2}{a}\sum_{n=1,3,5,\ldots} \mathrm{li}[(a/\rho_0)^n], \tag{3}$$

with li(x) the logarithmic integral function.[31] This expression, the authors state, provides the correct behavior of the force both far and near the surface of the nanotube, where it should resemble that of a metallic planar surface. It should be noted that the exact expression of Eq. (2) yields the correct limit for $\rho_0 \to a$, namely, $F(\rho_0) \approx 1/|\rho_0 - a|^2$, provided that the number of terms in the sum is sufficiently large. As can be seen in the figure, the behaviors of the exact potential and the approximation are qualitatively similar for distances far from the metal surface ($\rho_0/a \gg 1$). Near the surface, however, the exact potential diverges at a lower rate than the approximation. Since the tubular image states we are studying are located far from the surface,[23] it might be thought that differences near the surface should not affect them. Yet, these differences are large enough to affect the energy levels, as we will see in the following sections.

III. IMAGE POTENTIAL STATES

We use the exact form of the image potential [Eq. (2)] for a metallic cylinder to solve the Schrödinger equation and obtain the eigenvalues and eigenfunctions of the system. Since the image potential depends only on the radial distance, we can treat the problem using an effective potential that includes the repulsive centrifugal term:[32]

$$V_{\mathrm{eff}}(\rho_0) = V_{\mathrm{im}}(\rho_0) + \frac{l^2 - \frac{1}{4}}{2\mu\rho_0^2}\hbar^2. \tag{4}$$

Here μ is the reduced mass of the charged particle ($\mu = 1$ in atomic units) and l stands for the angular momentum quantum number. For sufficiently large l, the centrifugal potential provides a barrier that prevents the external charge from collapsing into the surface. In Fig. 3 we show the effective potential for different values of l and the same tube radius used in Fig. 2. Bound states form in the well between the repulsive barrier and the long-range image interaction. Our results show that the minimum l that supports bound states is $l_{\mathrm{min}} = 5$, in contrast with Granger's result of $l_{\mathrm{min}} = 6$. Furthermore, it is important to mark that, although our barrier for $l = 5$ is low (≈60 meV), the depths of the potential wells we obtain are quite different from those using the approximation of Eq. (3) (see Fig. 4), and these differences will affect the binding energies.

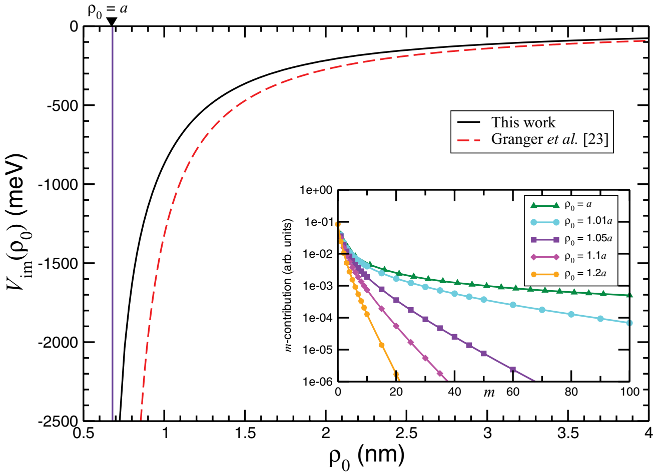

FIG. 2. (Color online) Image potential V_{im} as a function of the radial distance ρ_0 for a nanotube of radius $a = 0.68$ nm. Continuous black line, exact potential [Eq. (2)]; dashed red line, Granger's model [Eq. (4)]. Inset: a detail of the terms contributing to the sum in Eq. (2) as a function of m, for a series of values of distances ρ_0 relative to the tube's radius a.

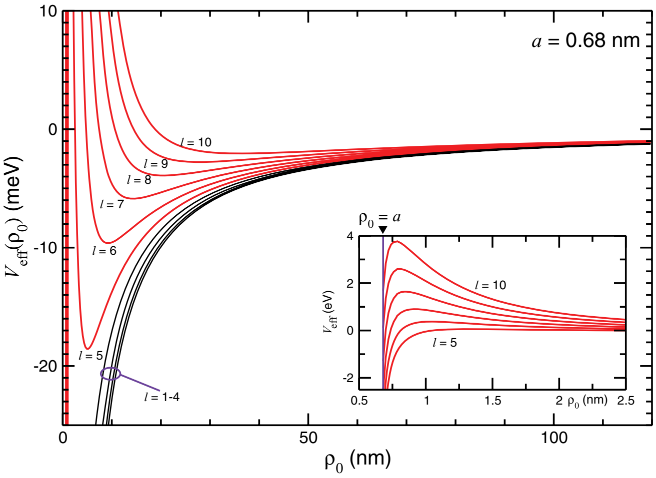

FIG. 3. (Color online) Effective potential V_{eff} seen by an electron situated at a radial position ρ_0 in front of a metallic nanotube of 0.68-nm radius. The first angular momenta supporting bound states are shown in red, $l = 5,6,\ldots 10$, for which potential wells are combined with the centrifugal barriers (shown in detail in the inset).

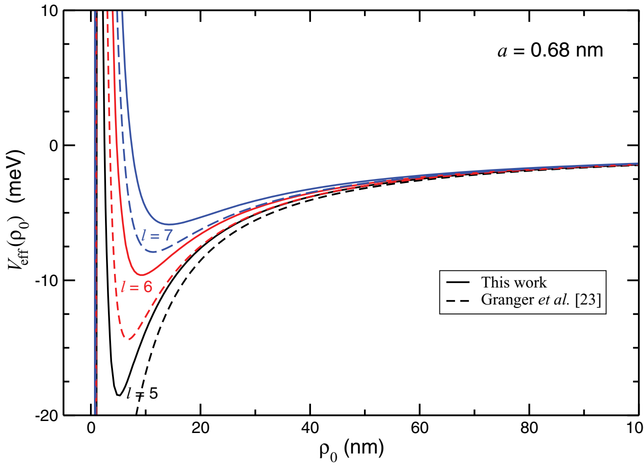

FIG. 4. (Color online) Effective potential $V_{\rm eff}$ for the lower angular momenta that support bound states, compared with Granger's results.

We assume that the electron wave function can be written in a separable form:

$$\Psi_{n,l,k}(\rho,\varphi,z)=\frac{\psi_{n,l}(\rho)}{\sqrt{\rho}}\,\frac{e^{il\varphi}}{\sqrt{2\pi}}\,\phi_k(z), \tag{5}$$

with the motion along the z direction (the tube's axis) independent from the transversal motion[23,27] in such a way that the total energy can be written as $E_{n,l,k}=E_{n,l}+E_k$. With this, the radial part of the Schrödinger equation becomes

$$\left\{\hbar^2\frac{d^2}{d\rho^2}+2\mu[E_{n,l}-V_{\rm eff}(\rho)]\right\}\psi_{n,l}(\rho)=0. \tag{6}$$

We have solved this equation numerically using the Numerov's shooting method. Figure 5 shows the wave functions for the $a=0.68$ nm tube, obtained for different values of the quantum numbers n and l. In the top panel, the first six bound states ($l=5,\dots,11$) corresponding to $n=1$ are displayed with continuous lines; the functions are normalized with the condition $\int|\psi_{n,l}(\rho)|^2\,d\rho=1$. We have included the functions obtained from Granger's potential for comparison (dashed lines). As can be seen, the shapes of the wave functions are very similar but the positions and amplitudes of their maxima are different. As expected, the lower angular momenta show the larger differences. In the bottom panel we plot, for $l=6$, the ground $n=1$ and first excited $n=2,3,4$ states as radial probability densities $|\Psi_{n,l,k}|^2$ around the tube.

Figure 6 shows a comparison of the binding energies obtained with the exact potential and with the approximated potential from Ref. 23. Our results are detailed in Table I. They still present, for fixed n, the l^{-3} behavior noticed for the approximate calculation, but the differences are important (30–40% for the deeper bound states), especially taking into account the low energies involved.

IV. SCALING PROPERTIES AND THE *l* BARRIER

A close inspection of the effective potential Eq. (4) suggests the exploration of the scaling properties of the system in order to obtain a general framework for the study of tubular image states. Equation (2) for the image potential can be rewritten as a function of ρ_0/a:

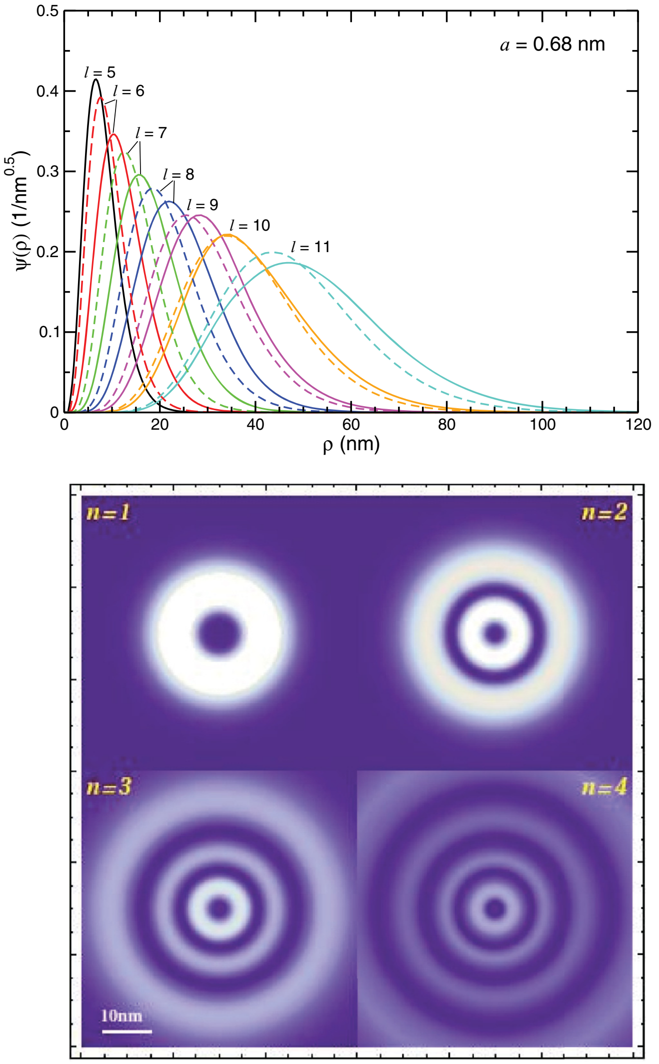

FIG. 5. (Color online) Top: radial wave functions $\psi_{n,l}(\rho)$ for $n=1$ corresponding to a metallic nanotube with $a=0.68$ nm, calculated with the exact induced potential (continuous line); Granger's potential wave functions are included in dashed lines. Bottom: density plots showing the probability function $|\Psi_{n,l,k}|^2$ around the same nanotube, for the states with angular momentum $l=6$, and principal quantum number $n=1$, 2, 3, and 4.

$$\begin{aligned}V_{\rm im}(\rho_0)&=\frac{1}{2}e\Phi_{\rm ind}(\rho_0,0,0)\\&=-\frac{e^2}{a}\frac{1}{\pi}\sum_{m=-\infty}^{\infty}\int_0^{\infty}d\zeta\,\frac{I_m(\zeta)}{K_m(\zeta)}\left[K_m\!\left(\zeta\frac{\rho_0}{a}\right)\right]^2,\end{aligned} \tag{7}$$

where we have replaced k by the dimensionless variable $\zeta=ka$ inside the integral. We can then define $x=\rho_0/a$ and write the image potential in terms of a dimensionless potential $\widetilde{V}_{\rm im}(x)$:

$$V_{\rm im}(\rho_0)=\frac{e^2}{a}\widetilde{V}_{\rm im}(x), \tag{8}$$

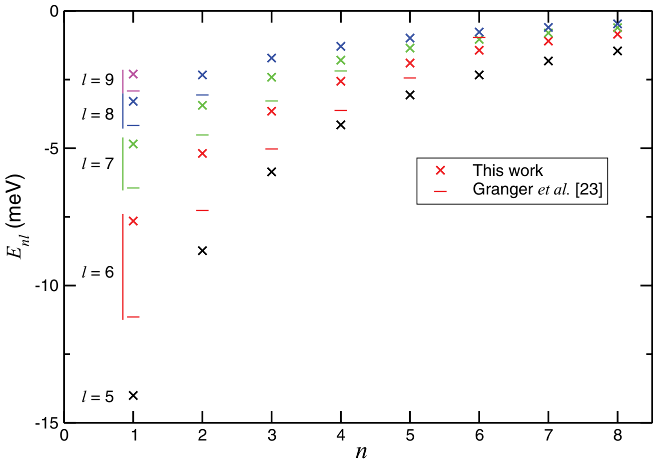

FIG. 6. (Color online) Binding energies $E_{n,l}$ obtained for a 0.68-nm-radius metallic nanotube for the exact image potential [Eq. (2)] (crosses); included are states with principal quantum number n up to eight, with different colors representing the different series of angular momenta l. Results using the approximated potential [Eq. (3)] are represented by dashes.

with

$$\widetilde{V}_{\rm im}(x) = -\frac{1}{\pi}\sum_{m=-\infty}^{\infty}\int_0^{\infty} d\zeta\, \frac{I_m(\zeta)}{K_m(\zeta)}[K_m(\zeta x)]^2. \tag{9}$$

In the same way, the effective potential Eq. (4) can be written in terms of a dimensionless effective potential $\widetilde{V}_{\rm eff}(x)$ as

$$V_{\rm eff}(\rho_0) = \frac{e^2}{a}\widetilde{V}_{\rm eff}(x), \tag{10}$$

with

$$\widetilde{V}_{\rm eff}(x) = \widetilde{V}_{\rm im}(x) + \frac{\lambda_l}{x^2}. \tag{11}$$

Here the parameter λ_l is given by

$$\lambda_l = \frac{\left(l^2 - \frac{1}{4}\right)}{2\mu e^2 a}\hbar^2. \tag{12}$$

Using the variable x, we can rewrite the Schrödinger equation for the image states in terms of this parameterized potential as

$$\frac{d^2\psi}{dx^2} - \widetilde{V}_{\rm red}(x)\psi + \widetilde{E}_{n,l}\psi = 0, \tag{13}$$

TABLE I. Binding energies (in meV) for a 0.68-nm-radius nanotube obtained with the exact image potential given in Eq. (2).

	l			
n	5	6	7	8
1	−14.005	−7.651	−4.845	−3.294
2	−8.731	−5.189	−3.438	−2.33
3	−5.861	−3.652	−2.415	−1.715
4	−4.149	−2.562	−1.794	−1.29
5	−3.060	−1.899	−1.353	−0.989
6	−2.331	−1.432	−1.036	−0.768
7	−1.823	−1.097	−0.803	−0.601

with the reduced potential and energies (in units of length^{-2})

$$\widetilde{V}_{\rm red}(x) = \beta\left[\widetilde{V}_{\rm im}(x) + \frac{\lambda_l}{x^2}\right], \tag{14}$$

$$\widetilde{E}_{n,l} = \frac{2ma^2}{\hbar^2}E_{n,l} = \frac{a^2}{a_0^2}\frac{E_{n,l}}{Ry}. \tag{15}$$

Here $a_0 = \hbar^2/me^2$ is the Bohr radius and $Ry = e^2/2a_0$ is the Rydberg unit (13.6 eV). β is, in terms of the parameters,

$$\beta = \frac{2me^2}{\hbar^2}a = \frac{2a}{a_0}, \tag{16}$$

while λ_l can also be written as

$$\lambda_l = (l^2 - 1/4)\frac{a_0}{2a}. \tag{17}$$

Hence, the Schrödinger equation takes the form of Eq. (13) and the reduced potential $\widetilde{V}_{\rm red}(x)$ Eq. (14) has two parameters, β and λ_l, which depend only on the angular momentum number l and the reduced radius a/a_0. This yields the desired general framework to study the image state wave functions and energies and to determine the range of values of the parameters where convergent solutions exist. For instance, we can study the conditions for which the competition between the centrifugal barrier and the attractive image potential will allow for the appearance of bound states detached from the surface. Figure 7 shows the dimensionless potential $\widetilde{V}_{\rm eff}$ as a function of the reduced variable x for different values of λ_l, spanning the range where the potential well and the positive barrier appear. As can be seen, this happens around $\lambda_l \approx 0.9$ (though the relative width and height of the barrier at this point may still be too low to ensure that the transmission through it is negligible). For the typical radius $a = 0.68$ nm, the condition $\lambda_l \geqslant 0.9$ yields a minimum value of $l = 5$, which is what we have obtained in the preceding sections. For different values of the radius a, the corresponding minimum value of l may be determined in the same way using the scaling parameter λ_l of Eq. (17).

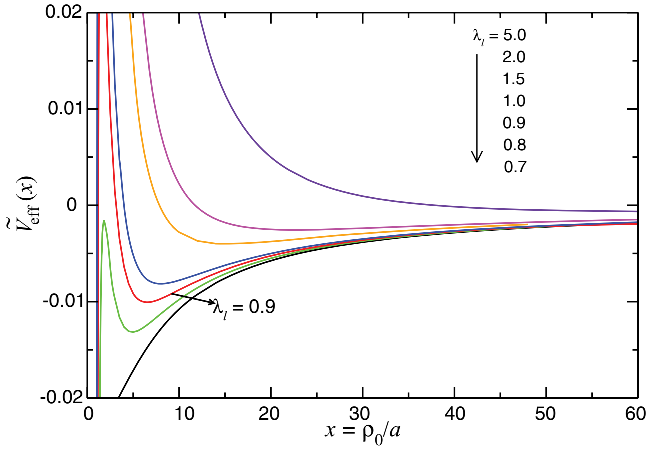

FIG. 7. (Color online) Reduced effective potential for different values of λ_l, from $\lambda_l = 0.7$ (bottom curve) to $\lambda_l = 5$ (top curve). The change of regime, with the formation of a positive centrifugal barrier, is observed to occur around $\lambda_l = 0.9$.

V. CARBON NANOTUBES

The preceding description is valid for infinite metallic cylindrical structures, either wires or nanotubes, with $\varepsilon \to \infty$. However, it is known that certain carbon nanotubes are not metallic but semiconducting, with energy gaps depending on their geometry.[33] For example, band-structure calculations for zig-zag nanotubes [characterized by a chiral vector $(n,0)$] show a zero energy gap when n is a multiple of three, while there is a finite gap otherwise. Also, metallicity depends on the diameter of the tube: curvature effects may give place to a secondary gap for sufficiently small diameters in $(n,0)$ and (n,m) nanotubes.[34]

Within the dielectric formulation, the image potential Eq. (2) for finite dielectric function ε scales as $1/\varepsilon$[30] (or $1/\sqrt{\varepsilon_i \varepsilon_j}$ for the anisotropic case of graphite). Hence, a nonmetallic tube will support image states only if ε is large enough. Unfortunately there are no reliable data for the value of the dielectric function of nanotubes in the static limit. Though data for the dielectric tensor of bulk graphite have been often used to evaluate the response function of nanotubes,[35,36] a macroscopically defined dielectric function ε may not be adequate for describing the response of an atomic-scaled structure such as a carbon nanotube.

An alternative, microscopic description of the behavior of valence electrons in a carbon nanotube is given by Mowbray *et al.*[37] Their two-fluid hydrodynamical model has been successfully applied to the description of plasmon excitations in a single-walled carbon nanotube.

This model describes the valence σ and π electrons in the nanotube as a superposition of two fluids with different densities, coupled through a Coulombic interaction. Following a (classical) hydrodynamical formulation, the potential induced at a position $\mathbf{r}$ by a charge e traveling parallel to the tube's axis at a distance ρ_0 $(>a)$ with velocity v is obtained as

$$\Phi_{\text{ind}}(\mathbf{r},t) = -4\pi e \sum_m \int \frac{dk}{\pi}\, e^{i\{m[\varphi-\varphi_0(t)]+k[z-z_0(t)-vt]\}} \times \frac{I_m(k\rho_<)K_m(k\rho_>)I_m(ka)K_m(k\rho_0)}{a^{-1}\chi_0^{-1}(m,ka,kv)+4\pi I_m(ka)K_m(ka)}. \quad (18)$$

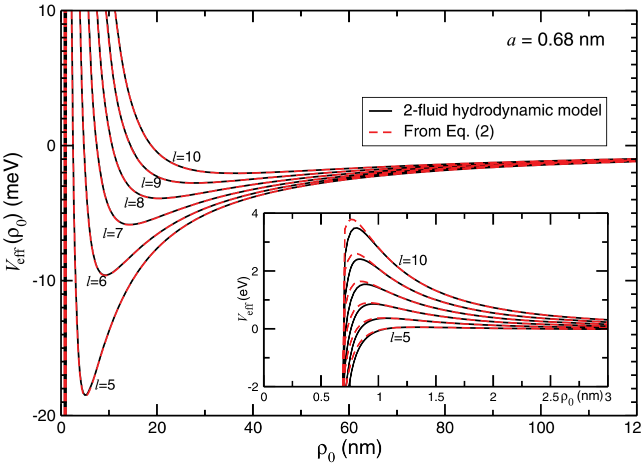

FIG. 8. (Color online) Effective potential V_{eff} as a function of the external charge position ρ_0 for the two-fluid hydrodynamic model in a metallic SWCNT of radius $a = 0.68$ nm. Also included are the results for a metallic tube using the image potential from Eq. (2).

Notice that it is evaluated at the resonant condition $\omega = kv$ for a parallel trajectory. Here, $\chi_0(m,\kappa,\omega)$ is the sum of the response functions of each fluid on the nanotube:

$$\chi_0(m,\kappa,\omega) = \chi_\sigma^0(m,\kappa,\omega) + \chi_\pi^0(m,\kappa,\omega), \quad (19)$$

with

$$\chi_\nu^0(m,k,\omega) = \frac{\frac{n_\nu^0}{m_\nu^*}(k^2+m^2/a^2)}{s_\nu^2(k^2+m^2/a^2)+\omega_{\nu r}^2-\omega(\omega+i\eta_\nu)}, \quad (20)$$

where, for each fluid, n_ν^0 and m_ν^* are the electron density and effective mass, η_ν is a damping constant, $\omega_{\nu,r}$ is a restoring frequency, and s_ν is the speed of propagation of density disturbances (see Ref. 37).

To obtain the image potential, analogous to Eq. (2), we evaluate the induced potential of Eq. (18) for a stationary electron situated at $(\rho_0,0,0)$ with $v = 0$. Hence we have

$$V_{\text{im}}^{\text{CN}}(\rho_0) = -4\pi e^2 \sum_m \int \frac{dk}{\pi} \times \frac{I_m^2(ka)K_m^2(k\rho_0)}{a^{-1}\chi_0^{-1}(m,ka,0)+4\pi I_m(ka)K_m(ka)}. \quad (21)$$

This expression reduces to Eq. (2) for $\chi_0^{-1} \to 0$.

The metallic character of a nanotube is given here through the values of the restoring frequencies $\omega_{\nu,r}$, which are directly related to the energy band gap for the corresponding valence electrons. In general, we can consider that the σ electrons behave as in a semiconductor, with a band gap of about 12 eV. In turn, the energy bands for π electrons may present finite or null gaps, depending on the geometry or, more specifically, the way the tube is rolled up.[33,38] In Ref. 37, the σ electrons were modeled with a restoring force $\omega_{\sigma,r} = 16$ eV, while for π electrons the authors took a semimetal approach, with $\omega_{\pi,r} = 0$ eV. Using these values, we calculated the effective potential as $V_{\text{eff}} = V_{\text{im}}^{\text{CN}} + (l^2 - 1/4)/(2\mu\rho_0^2)$.

Figure 8 shows a comparison of the effective potential curves for different angular momenta, compared with the results corresponding to metallic tubes. The differences are found to be negligible, especially in the region of the potential

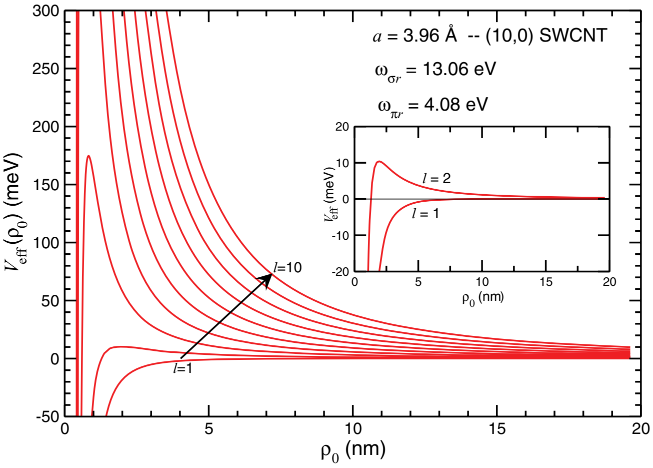

FIG. 9. (Color online) Effective potential for a SWCNT of radius $a = 3.96$ Å [zig-zag nanotube with chiral vector (10,0)] with $\omega_{\sigma,r} = 13.06$ eV and $\omega_{\pi,r} = 4.08$ eV.

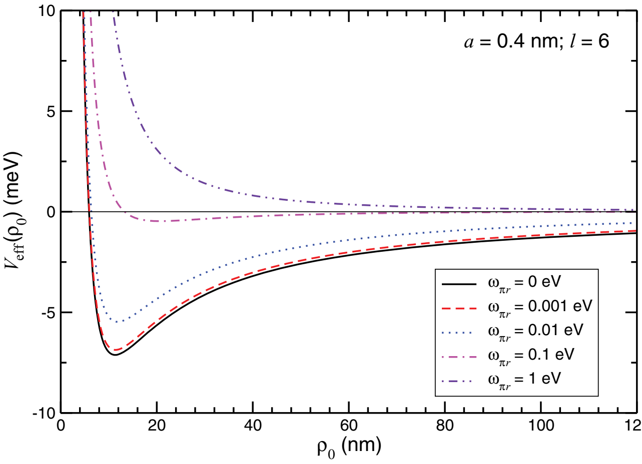

FIG. 10. (Color online) Effective potential for a SWCNT of radius $a = 0.4$ nm for angular momentum $l = 6$ and $\omega_{\sigma,r} = 13.08$ eV; $\omega_{\pi,r}$ is varied from 0 to 1 eV.

wells that support the bound states. Larger differences are observed near the nanotube (see inset), but these would not directly affect the bound states. This agreement is easily explained by inspecting the structure of the response function χ_0 and the two-fluid model. By using a value of $\omega_{\pi,r} = 0$, the (semi)metallic character of the π electrons prevails in the optical limit $\omega \to 0$ and is equivalent to the results obtained with $\varepsilon \to \infty$ for ideal metallic tubes in the preceding sections.

On the other hand, nonmetallic nanotubes can be characterized using finite values of the restoring frequencies of both fluids, in correspondence to band gaps for each geometric configuration yielding different chiralities. In order to have an estimation of how this would affect image potential states, we have calculated $V_{\rm eff}$ using the values given by Jovanović *et al.*[39] in their study of plasmon excitations in graphene mono- and multilayers. They have found that electron energy loss spectra recorded for energetic electrons are well reproduced by taking $\omega_{\sigma,r} = 13.06$ eV and $\omega_{\pi,r} = 4.08$ eV. These values are close to those used for C_{60} studies and are consistent with the calculated gaps for π bands in nanotubes.[38] Preliminary results also show that similar values should be used for carbon nanotubes in order to better reproduce energy loss experiments. With these values for restoring frequencies, we have obtained the curves shown in Fig. 9 for the effective potential. In order to study a representative case, these values were calculated for a (10,0) zig-zag nanotube, with radius $a = 0.396$ nm. As can be seen, the potential wells disappear and bound image states would not be supported. Of course, these values correspond to ε far from the "large enough" condition stated by Granger *et al.*[23] However, the approach presented here allows us to quantify this condition with realistic values of the response function for nonmetallic nanotubes. In order to have the potential well that gives rise to TIS, the π electrons restoring frequencies (and hence energy band gaps) should be as small as 10^{-2} eV; Fig. 10 shows the variation of the effective potential for $l = 6$ and different values of $\omega_{\pi r}$, from 0 to 1 eV, for $a = 0.4$ nm.

VI. CONCLUSIONS

In this work we have addressed the subject of tubular image potential states around metallic and nonmetallic nanotubes. Starting from the potential induced by a charged particle in front of a metallic cylindrical surface[30] we have solved the radial Schrödinger equation for the bound-state wave functions and obtained the energy series in analogy to Rydberg states in front of planar surfaces. Our results present significant differences from those presented by Granger *et al.* in Ref. 23, who used an approximate expression to account for the image potential. Although the largest differences between our formulation and Granger's occur in the region close to the cylinder's surface, these prove to be significant for the values of the binding energies, with differences up to 30–40%. We mark the sensitiveness of both eigenfunctions and eigenenergies to the image potential. Particularly, we stress the fact that differences between the asymptotic approximation and the exact potential in the region near the surface of the tube result in important corrections on bound states residing relatively far from it. An example of this is the $l = 5$ bound state which is suppressed in the approximate calculation. In this regard, we have also studied the scaling properties of the effective potential and the Schrödinger equation, providing a general way to assess the l barrier, i.e., the minimum value of angular momentum for which extended bound states can exist.

We have also presented a realistic formulation for evaluating the image potential in nonmetallic cases for carbon nanotubes, based on the hydrodynamical model for the response function of the π and σ electrons. This allows us to postulate that this kind of tubular image state will not appear in front of dielectric or semiconducting nanotubes with band gaps over 0.1 eV.

We expect that these results may be useful as a guide for the detection of these tubular image states and for the determination of their properties in different experimental conditions.

ACKNOWLEDGMENTS

We acknowledge partial financial support from Universidad Nacional de Cuyo (Grants No. 06/338 and No. 06/C345) and Consejo Nacional de Investigaciones Científicas y Técnicas (Grant No. PIP112 20090100670).

---

[1] V. Dose, W. Altmann, A. Goldmann, U. Kolac, and J. Rogozik, Phys. Rev. Lett. **52**, 1919 (1984).

[2] D. Straub and F. J. Himpsel, Phys. Rev. Lett. **52**, 1922 (1984).

[3] J. R. Goldman and J. A. Prybyla, Phys. Rev. Lett. **72**, 1364 (1994).

[4] J. Lehmann, M. Merschdorf, A. Thon, S. Voll, and W. Pfeiffer, Phys. Rev. B **60**, 17037 (1999).

[5] A. G. Borisov, T. Hakala, M. J. Puska, V. M. Silkin, N. Zabala, E. V. Chulkov, and P. M. Echenique, Phys. Rev. B **76**, 121402 (2007).

[6] M. Rohleder, W. Berthold, J. Güdde, and U. Höfer, Phys. Rev. Lett. **94**, 017401 (2005).

[7] I. Yamamoto, M. Mikamori, R. Yamamoto, T. Yamada, K. Miyakubo, N. Ueno, and T. Munakata, Phys. Rev. B **77**, 115404 (2008).

[8] Q. Yang, M. Muntwiler, and X.-Y. Zhu, Phys. Rev. B **80**, 115214 (2009).

[9] M. Zamkov, N. Woody, B. Shan, H. S. Chakraborty, Z. Chang, U. Thumm, and P. Richard, Phys. Rev. Lett. **93**, 156803 (2004).

[10] M. Feng, J. Zhao, and H. Petek, Science **320**, 359 (2008).

[11] J. Zhao, M. Feng, J. Yang, and H. Petek, ACS Nano **3**, 853 (2009).

[12] N. Armbrust, J. Güdde, P. Jakob, and U. Höfer, Phys. Rev. Lett. **108**, 056801 (2012).

[13] D. F. Padowitz, W. R. Merry, R. E. Jordan, and C. B. Harris, Phys. Rev. Lett. **69**, 3583 (1992).

[14] N. Fischer, S. Schuppler, R. Fischer, T. Fauster, and W. Steinmann, Phys. Rev. B **47**, 4705 (1993).

[15] D. Tang and D. Heskett, Phys. Rev. B **47**, 10695 (1993).

[16] M. Wolf, E. Knoesel, and T. Hertel, Phys. Rev. B **54**, R5295 (1996).

[17] S. Link, H. A. Dürr, G. Bihlmayer, S. Blügel, W. Eberhardt, E. V. Chulkov, V. M. Silkin, and P. M. Echenique, Phys. Rev. B **63**, 115420 (2001).

[18] K. Boger, M. Weinelt, and T. Fauster, Phys. Rev. Lett. **92**, 126803 (2004).

[19] C. Reuß, I. L. Shumay, U. Thomann, M. Kutschera, M. Weinelt, T. Fauster, and U. Höfer, Phys. Rev. Lett. **82**, 153 (1999).

[20] D. C. Marinica, C. Ramseyer, A. G. Borisov, D. Teillet-Billy, J. P. Gauyacq, W. Berthold, P. Feulner, and U. Höfer, Phys. Rev. Lett. **89**, 046802 (2002).

[21] A. D. Miller, I. Bezel, K. J. Gaffney, S. Garret-Roe, S. H. Liu, P. Szymanski, and C. B. Harris, Science **297**, 1163 (2002).

[22] P. Echenique, R. Berndt, E. Chulkov, T. Fauster, A. Goldmann, and U. Höfer, Surf. Sci. Rep. **52**, 219 (2004) .

[23] B. E. Granger, P. Král, H. R. Sadeghpour, and M. Shapiro, Phys. Rev. Lett. **89**, 135506 (2002).

[24] M. Zamkov, H. S. Chakraborty, A. Habib, N. Woody, U. Thumm, and P. Richard, Phys. Rev. B **70**, 115419 (2004).

[25] G. Gumbs and A. Balassis, Phys. Rev. B **71**, 235410 (2005).

[26] G. Gumbs, A. Balassis, and P. Fekete, Phys. Rev. B **73**, 075411 (2006).

[27] G. A. Bocan, N. R. Arista, J. L. Gervasoni, and S. Segui, Phys. Rev. B **77**, 035438 (2008).

[28] K. Schouteden, A. Volodin, D. A. Muzychenko, M. P. Chowdhury, A. Fonseca, J. B. Nagy, and C. Van Haesendonck, Nanotechnology **21**, 485401 (2010).

[29] The derivation is valid for any charged particle q; we particularize it for electrons since it is the most commonly used spectroscopy in surface studies related to image states.

[30] J. L. Gervasoni and N. R. Arista, Phys. Rev. B **68**, 235302 (2003).

[31] M. Abramowitz and I. Stegun, eds., *Handbook of Mathematical Functions* (Dover, New York, 1970).

[32] E. Merzbacher, *Quantum Mechanics*, 2nd ed. (Wiley, New York, 1970).

[33] R. Saito, G. Dresselhaus, and M. Dresselhaus, *Physical Properties of Carbon Nanotubes* (Imperial College Press, London, 1998).

[34] T. W. Odom, J.-L. Huang, P. Kim, and C. M. Lieber, J. Phys. Chem. B **104**, 2794 (2000).

[35] T. Stöckli, Z. L. Wang, J.-M. Bonard, P. Stadelmann, and A. Châtelain, Philos. Mag. B **79**, 1531 (1999).

[36] O. Stéphan, D. Taverna, M. Kociak, K. Suenaga, L. Henrard, and C. Colliex, Phys. Rev. B **66**, 155422 (2002).

[37] D. J. Mowbray, S. Segui, J. Gervasoni, Z. L. Mišković, and N. R. Arista, Phys. Rev. B **82**, 035405 (2010).

[38] J. D. Correa, A. J. R. da Silva, and M. Pacheco, J. Phys. Condens. Matter **22**, 275503 (2010).

[39] V. B. Jovanović, I. Radović, D. Borka, and Z. L. Mišković, Phys. Rev. B **84**, 155416 (2011).